



OPEN X-ray microscopy and talbot imaging with the matter in extreme conditions X-ray imager at LCLS

Eric Galtier^{1✉}, Hae Ja Lee¹, Dimitri Khaghani¹, Nina Boiadjieva¹, Peregrine McGehee¹, Ariel Arnott¹, Brice Arnold¹, Meriame Berboucha^{1,2}, Eric Cunningham¹, Nick Czapla¹, Gilliss Dyer¹, Robert Ettlbrick¹, Philip Hart¹, Philip Heimann¹, Marc Welch¹, Mikako Makita³, Arianna E. Gleason¹, Silvia Pandolfi^{1,4}, Anne Sakdinawat¹, Yanwei Liu¹, Michael J. Wojcik⁵, Daniel Hodge⁶, Richard Sandberg⁶, Maria Pia Valdivia⁷, Victorien Bouffetier⁸, Gabriel Pérez-Callejo⁹, Frank Seiboth¹⁰ & Bob Nagler¹

The last decade has shown the great potential that X-ray Free Electron Lasers (FEL) have to study High Energy Density (HED) physics. Experiments at FELs have made significant breakthroughs in Shock Physics and Dynamic Diffraction, Dense Plasma Physics and Warm Dense Matter Science, using techniques such as isochoric heating, inelastic scattering, small angle scattering and X-ray diffraction. In addition, and complementary to these techniques, the coherent properties of the FEL beam can be used to image HED samples with high fidelity. We present new imaging diagnostics and techniques developed at the Matter in Extreme Conditions (MEC) instrument at Linac Coherent Light Source (LCLS) over the last few years. We show results in Phase Contrast Imaging geometry, where the X-ray beam propagates from the target to a camera revealing its phase, as well as in Direct Imaging geometry, where a real image of the sample plane is produced in the camera with a spatial resolution down to 200 nm. Last, we show an implementation of the Talbot Imaging method allowing both X-ray phase and intensity measurements change introduced by a target with sub-micron resolution.

High Energy Density (HED) science has traditionally made ample use of X-ray radiography and imaging to investigate a variety of phenomena, such as the implosions of inertial confinement fusion (ICF) capsules^{1–7}, X-pinch plasmas^{8–11} and the general hydrodynamics of evolution of HED targets^{12,13}. Since the creation of these conditions involves the destruction of the targets in so-called *single shot* experiments, bright X-ray pulses are needed to obtain quantitative data. Historically, X-ray sources generated by the interaction of high power laser with backlighter targets have been employed, with typical spatial and temporal resolution on the order of tens of micrometers and hundreds of picoseconds or more^{12,14}. Phase Contrast Imaging techniques with backlighters have thus been performed to study the dynamics of mm-scale targets^{15–23}, while synchrotrons have reached sub-micron resolutions usually on static samples^{24,25}.

The start of operation of LCLS²⁶ in 2009 opened new possibilities for X-ray imaging in HED science. The coherent properties of the beam allow for imaging with sub-micron spatial resolution, while the short, bright pulses allow temporal resolution of tens of femtoseconds. These combined properties allow for single-shot X-ray imaging techniques to emerge as a leading technique to further our understanding of complex HED phenomena. At LCLS, the Matter in Extreme Conditions endstation²⁷ is specifically tailored to field experiments in HED science. To foster this field of research, the different imaging techniques and instruments have been developed, and are available to its user community.

¹SLAC National Accelerator Laboratory, 2575 Sand Hill Rd., Menlo Park, CA 94025, USA. ²Plasma Physics, Imperial College London, London SW7 2AZ, UK. ³European XFEL, Holzkoppel 4, 22869 Schenefeld, Germany. ⁴Sorbonne University, Paris, France. ⁵Argonne National Laboratory, 9700 S. Cass Avenue, Lemont, IL 60439, USA. ⁶Department of Physics and Astronomy, Brigham Young University, Provo, UT 84602, USA. ⁷Center for Energy Research, University of California San Diego, San Diego, CA, USA. ⁸ALBA-CELLS Synchrotron Radiation Facility, 08290 Cerdanyola del Vallès, Barcelona, Spain. ⁹Departamento de Física Teórica Atómica y Óptica, Universidad de Valladolid, 47011 Valladolid, Spain. ¹⁰Center for X-ray and Nano Science, Deutsches Elektronen-Synchrotron DESY, Notkestraße 85, 22607 Hamburg, Germany. ✉email: egaltier@slac.stanford.edu

In this paper, we describe the use and performances of the MEC X-ray Imager (MXI) and the different diagnostic imaging techniques that make use of it, and present preliminary proof of principle experiments to showcase its potential for HED science.

Instrument overview

The MXI instrument has two main components: an in-vacuum X-ray lens stack holder and an in-air optical microscope, as detailed in Fig. 1.

The in-vacuum component is designed for use in the MEC target chamber (technical details on the endstation can be found in Ref.²⁷). It uses compound refractive Beryllium lenses (Be CRL) to focus the X-ray beam to sub-micron spot sizes. The capabilities of such lens stacks have been described extensively in the literature^{28–31}, and have been used for this purpose at MEC^{32–34}. A stack of lenses is placed on alignment stages that positions the lenses in the beam. Up to three stacks of lenses can be placed on the instrument simultaneously, to allow usage of different photon energies and/or focal lengths during an experiment without venting the MEC vacuum chamber. The front stack can accommodate up to 100 lenses, necessary for the higher photon energies. The lens stacks are mounted on a hexapod, allowing for precise alignment with six degrees of freedom: the translations are aligned with the LCLS orthogonal coordinate system and rotation around each of these axis. The hexapod is attached to a linear translation stage with 500 mm travel range to change the distance between the lens stack and the object plane along the LCLS X-ray beam.

Two thin pins are precisely located with respect to the Be CRL stacks on the lens platform and are far from each other along the FEL direction to maximize alignment accuracy. They are initially used for the pre-alignment in air with the reference optical laser collinear with the FEL, and later, in vacuum conditions using the FEL itself via their shadowgraphy on the detector. These pins are critical to allow for a fast while precise alignment, typically achieved in less than 30 min.

Since stacks of Be lenses are known to have aberrations, which can limit their use in imaging and phase contrast application, a phase plate that corrects these aberrations³⁴ can be placed 10 mm in front of the lens set. The phase plate is aligned in the horizontal and vertical direction with two small linear stages, which can also completely retract the corrector. The MXI lens sets can be placed either upstream of the sample (see “Phase contrast imaging geometry” section) for phase contrast imaging or downstream (see “Direct imaging geometry” section) for direct imaging of a sample.

In typical HED experiments, samples are driven by the MEC short or long pulse laser orthogonally to the imaging direction (e.g., a shock is imaged traveling through a sample). To this end a sample holder allowing such geometry is available (see Fig. 2).

The samples are aligned to TCC with better than 20 μm accuracy using two long-distance telescopes (see²⁷ for details), which view the sample at orthogonal directions. The MXI can be used to further improve the alignment accuracy down to better than 1 μm in the plane perpendicular to the FEL. The samples are mounted on a pillar that is screwed to the sample holder. The pillars are designed to accommodate for line of sight of additional scientific diagnostics (e.g. for use in shock experiment to allow for VISAR³⁵ measurements on thin samples).

The image is recorded on the in-air component of the MXI, an X-ray camera that is placed behind the MEC chamber. The camera can be placed between 1.3 and 4.3 m behind the sample plane. For the large propagation distance, a fly tube is inserted and terminated by a 125 μm thick kapton window to maintain low scattering and absorption transport conditions for the X-ray beam. In general, the farthest distance is preferred to have the largest magnification, although some application may benefit from the shorter distance (i.e., ptychography³⁶).

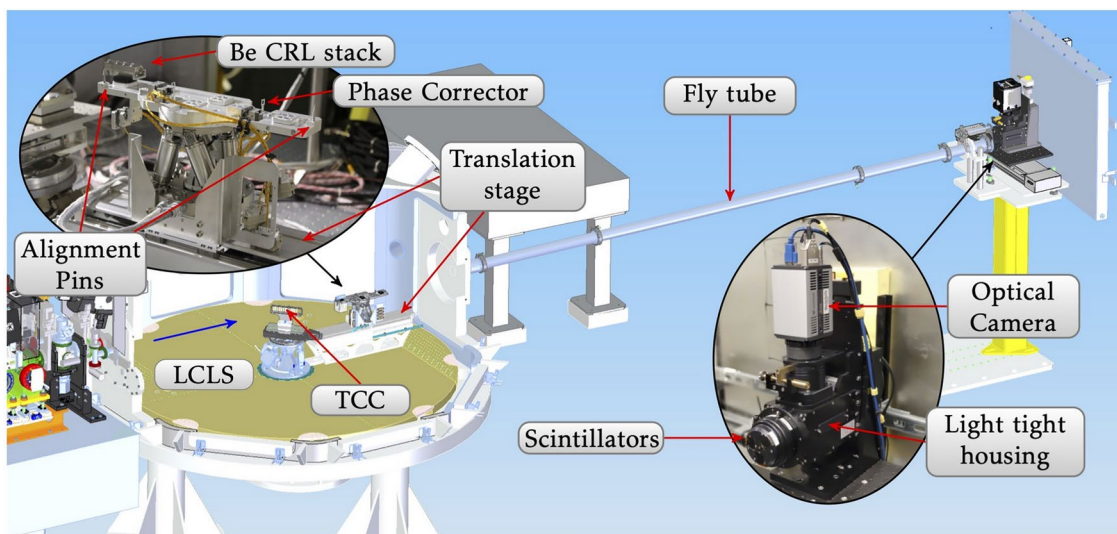


Fig. 1. Overview of the MXI system at MEC in Direct Imaging geometry with the indirect X-ray detector placed about 4 m from TCC behind a fly tube. TCC is Target Chamber Center, the interaction point between the LCLS and the optical lasers.

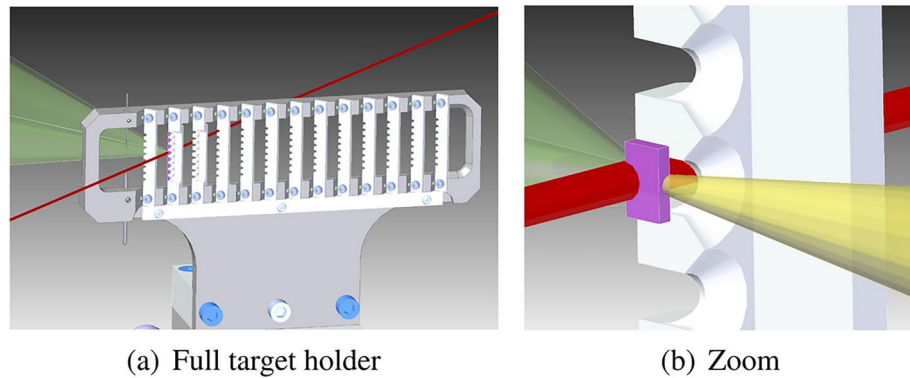


Fig. 2. (a) 3D model of the target holder with an orthogonal configuration between the long pulse drive laser (in green) and the X-rays (in red). (b) Zoom in of a single target on a pillar suitable for use with the MEC VISAR diagnostic²⁷ (VISAR beam in yellow).

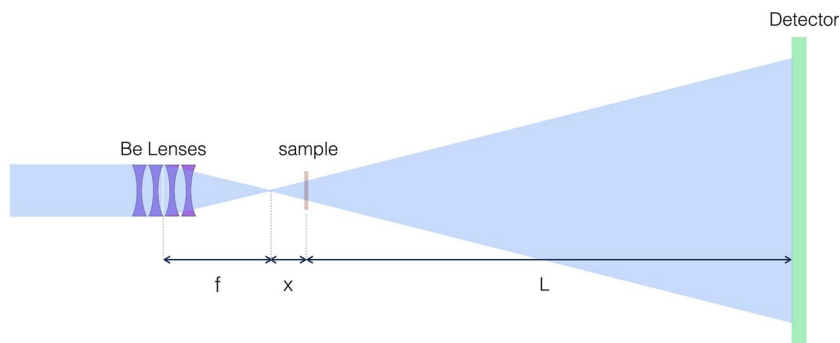


Fig. 3. Sketch of the MXI setup in phase contrast imaging (PCI) geometry.

For most experiments, we have used an indirect X-ray imaging Optique Peter microscope³⁷, consisting of three options of Ce:GAGG scintillators and three options of high-numerical aperture infinity-corrected optical microscope objectives ($\times 2$, $\times 4$ and $\times 10$ magnification) to further choose between high-magnification or large field-of-view. This assembly is coupled to an Andor Zyla 5.5 sCMOS optical camera, which has a pixel size of $6.5 \mu\text{m}$. Direct imaging cameras (e.g., ePix or Jungfrau) can be used instead, however the resolution is limited by the pixel size ($100 \mu\text{m}$ for ePix10k, $50 \mu\text{m}$ for ePix100 and $75 \mu\text{m}$ for Jungfrau). In addition, multiframe X-ray cameras developed by hCMOS³⁸ with pixel size of $25 \mu\text{m}$ ^{39–41} and capable of capturing multiple image frames spaced as little as 2 ns apart, can also be used, in conjunction with the LCLS multi-bunch operation mode^{42,43}. An advantage of direct detection compared to scintillator based detection is that these cameras are orders of magnitude more sensitive, and therefore can be used with thicker, higher Z, more absorptive samples.

Phase contrast imaging geometry

The imaging geometry first deployed at MEC⁴⁴ used a diverging beam at target and optic-free propagation from target to detector plane. A schematic of the setup can be seen in Fig. 3.

The MXI, with a lens set of focal length f , is placed in the MEC vacuum chamber and focuses the LCLS beam to approximately 100 nm. A certain distance, x , behind the focus, a sample is placed in the divergent beam. The X-ray beam propagates to a detector at a distance L behind the sample, leading to a geometric magnification of the sample of $\frac{L}{x}$. Due to the long propagation distance of the X-ray, phase difference induced by the sample can readily be seen in the image (e.g., clear fringes appear at sharp phase boundaries). Iterative algorithms can be used to retrieve the phase, and if this is successful, the full complex transmission function (i.e., absorption and phase shift) can be calculated. Experiment in this geometries have been fielded at MEC, yielding scientific results on shockwave propagation in diamond⁴⁴ and the kinetics of phase transformations in silicon⁴⁵. The setup can be easily combined with X-ray diffraction. Moving the lenses of the MXI closer to the target reduced the field of view of the image, and therefore the area where X-rays hit the target. In this way, diffraction from an area of only a few microns in size can be obtained, and different crystallographic phases in the sample can be identified⁴⁵. A typical image of a laser-generated shock wave traveling through a sample can be seen in Fig. 4 and more examples have been published in e.g.^{27,32,44}.

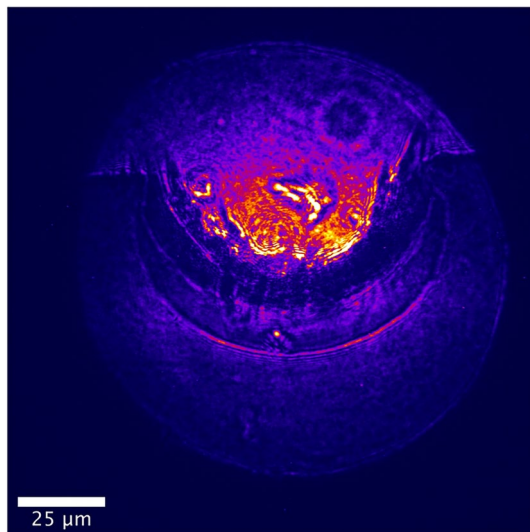


Fig. 4. The MEC long pulse laser impinges on a plastic ablator coated on a Si target. An elastic shock front, followed by a plastic deformation front indicative of material compression travels from top to bottom. Ablator ejecta coming out of the vacuum-ablator interface are also observed. This raw data, background subtracted only, was taken 20 ns after 8 J of a 10 ns long optical laser pulse hit the ablator. For this image, the X-ray free electron laser delivered 2.5 mJ at the photon energy of 8.2 keV with the SASE bandwidth.

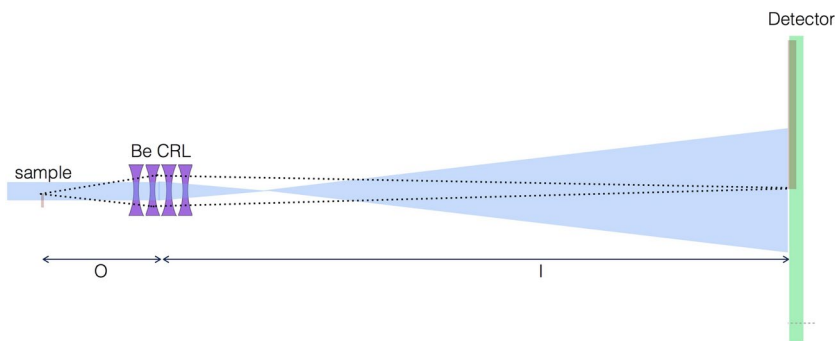


Fig. 5. MXI in direct imaging geometry.

Direct imaging geometry

While the PCI geometry described above has great potential when a full phase retrieval can be performed, it proves to be challenging for HED samples. Without such a phase retrieval, the resolution can be severely limited, and an alternative setup that directly images a sample on the detector has been developed and used at MEC. A sketch of the setup is shown in Fig. 5.

In this geometry the Be lenses are placed behind the sample such that the distance to the sample, O , and the distance to the camera, I , matches the well known thin lens formula $\frac{1}{O} + \frac{1}{I} = \frac{1}{f}$, with f the focal length of the Be lenses. Such a setup allows for imaging intensity contrast of the sample with sub-micron resolution, even when phase reconstruction is not possible.

The MXI instrument was tested in the direct imaging geometry at 8.2 keV, 9.5 keV and 18 keV photon energy. For 8.2 keV and 9.5 keV, a set of 25 Beryllium lenses with a curvature of 50 μm were used. At 8.2 keV (9.5 keV), the set has a focal length of 204 mm (264 mm) and was placed 214 mm (281 mm) downstream of the target, leading to an image at the detector, placed 4.3 m behind the lenses, with a magnification of approximately $\times 20$ ($\times 15$). The position of the lenses was tuned to get the best imaging resolution, using resolution targets. Images of the resolution target are shown in Fig. 6. Where the line widths are separated by 200 nm, we measure a contrast better than 30%, which means that these features are resolve according to the Rayleigh criterion.

At photon energies as high as 18 keV, the setup and alignment is more sensitive since many more Be lenses are needed. In addition, the shortest focal length that can be used is generally larger, leading to a smaller magnification. Nevertheless, the higher photon energy allows using either thicker targets, or targets containing higher Z-elements, while maintaining enough transmission to collect high-quality images. We demonstrated its use with a lens stack of 98 lenses of 50 μm radius of curvature at their apex, leading to a focal length of 266 mm

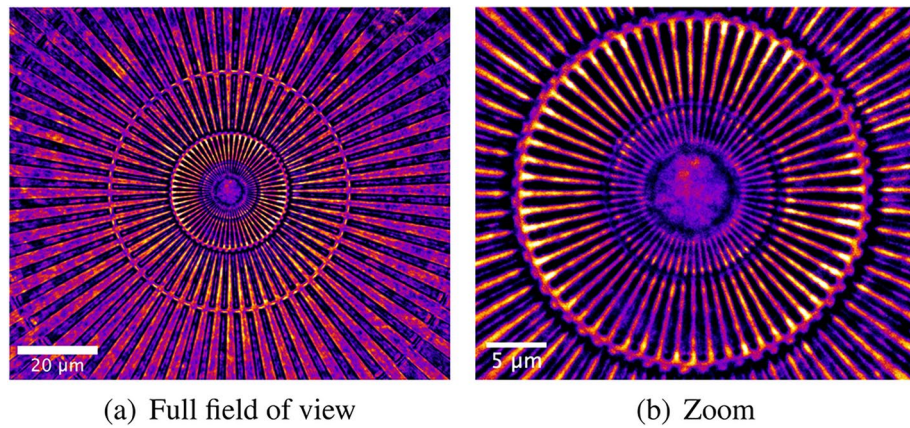


Fig. 6. Background subtracted image of a Siemens star resolution target at 9.5 keV in a false color scale. **(a)** Full field of view of $110\ \mu\text{m} \times 93\ \mu\text{m}$. **(b)** Zoom of the center. The smallest features near the center of the picture have a spacing of 200 nm, resulting in an effective pixel size of about 0.045 nm/px.

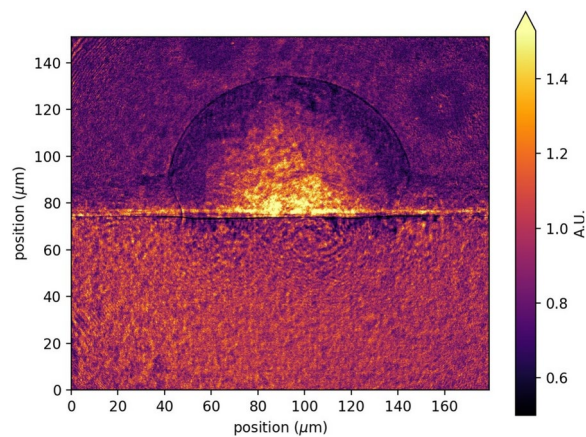


Fig. 7. White-Field corrected image of a shock wave propagating through a silicon sample. The MEC short pulse laser, with pulse length of 45 fs and energy of 1 J was focused down to a spot of $7\ \mu\text{m}$ diameter on the edge of a Si wafer, $100\ \mu\text{m}$ thick in the X-ray direction. The image is taken 2 ns after the laser strikes the target. We can clearly observe the propagation of the near-spherical expanding shock wave originating from the laser/surface interaction, as well as compressed (darker) material just behind the shock front. The target is set between about 70 and $150\ \mu\text{m}$ on the vertical axis, while the rest is vacuum.

and a magnification of $\times 15$. Measurement on resolution targets showed a resolution similar to 8.2 keV and 9.5 keV.

Examples of the use of the MXI in direct imaging geometry are detailed below. In Fig. 7 a shockwave in a silicon sample, driven by the MEC short pulse laser is depicted.

This geometry is compatible with both the long pulse and the short pulse laser systems available at MEC, as well as a suite of X-ray and optical diagnostics (e.g. X-ray Diffraction, VISAR, X-ray spectroscopy, optical polarimetry) making it an ideal technique to obtain a complete picture of the dynamics happening in HED samples.

The imaging setup can also be used to measure the spot size of the standard beryllium focusing lenses that are in the MEC beamline. These lenses sit approximately 4.2 m upstream of the center of the MEC target chamber (see²⁷ for details), and therefore a stack with focal length between 3.9 and 4.4 m is generally used for standard MEC experiment, with a best focus around $1.2\ \mu\text{m}$. Wavefront measurement have in the past been performed of such lens stack, showing significant spherical aberrations, generating ring-patterns around the focus⁴⁶. The MXI direct imaging geometry can be used to image the intensity profile of the X-ray beam on the sample. In Fig. 8, we show the intensity profile around the focus of our beamline lenses as imaged by the MXI instrument. The airy-like ring pattern can be clearly seen. This type of measurement is of importance for all optical pump—X-ray probe experiments where X-rays are usually being used out of focus in the hope of illuminating a more uniform area. Our high-resolution imager shows, through the measurement of the X-ray caustic profile, that it might not be the case.

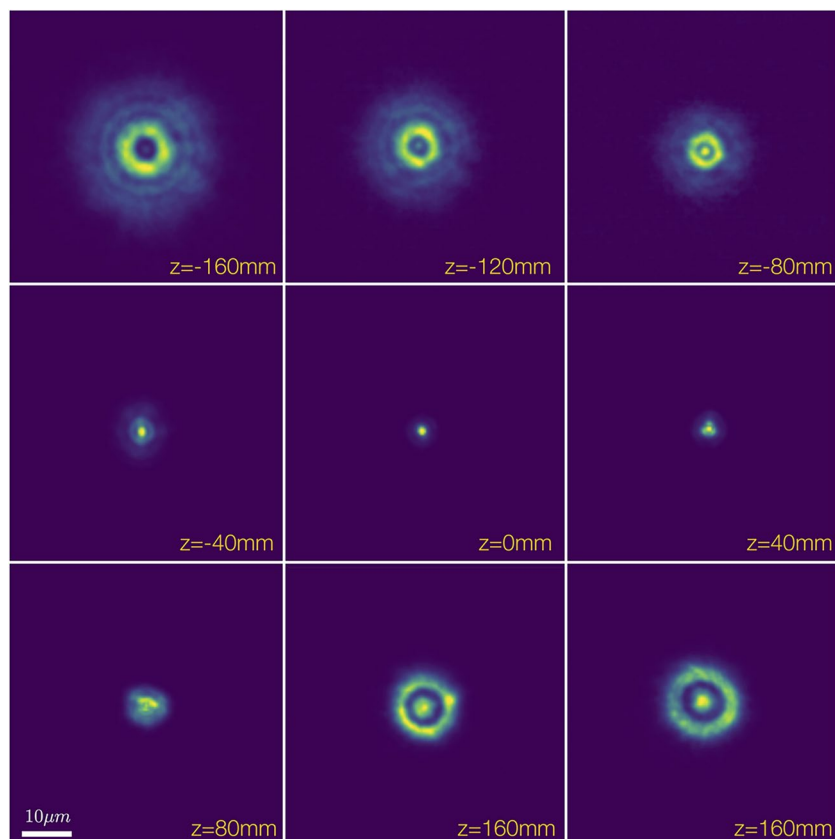


Fig. 8. Intensity profile of the focus of the MEC beamline lenses in steps of 40 mm. A set of 7 Be lenses with curvature of 300 μm at their apex, leading to a focal length of 4.22 m was chosen. 800 μm pinhole were placed in before and after the lens set to restrict the X-ray to the useful aperture of the lenses.

Parameter	Value	Unit
Photon energy	5–24	keV
Repetition rate	On demand–120 ^a	Hz
Pulse duration	< 20–50	fs
X-ray magnification	$\times 5$ – $\times 40$	–
Total magnification ^b	$\times 7$ – $\times 400$	–
Field of view	50–300	μm
Beam mode	SASE, seeded ^c , multipulse ^d	–

Table 1. Summary of the specifications of the MXI. ^a120 Hz is compatible with X-ray cameras only. It is typically used at 30 Hz maximum for alignment. Otherwise, it matches the optical laser repetition rate. ^bCombination of X-ray and Optical magnification. ^cReduces chromatic aberrations but lowers the input X-ray pulse energy. ^dWith use of the hCMOS detector.

Table 1 summarizes the working envelop of the MXI and its expected performances in direct imaging mode. The device can provide high resolution X-ray imaging over the full X-ray energy range available at MEC, albeit at varying resolution and magnification which are a function of the incoming photon energy. The total magnification is a combination of the X-ray magnification provided by the Be CRL in vacuum (this mainly constrains the diffraction limited performances), and the optical magnification provided by the objective used in the Optique Peter assembly (this allows for oversampling of the X-ray images).

Talbot imaging

A special capability of using the MXI in direct imaging mode is its compatibility with Talbot interferometry^{47,48}. Considering the MXI capabilities and the applications of interest like Warm Dense Matter (WDM) and High Energy Density Plasmas (HEDP) studies, different phase retrieval methods can be employed (see the references on Talbot imaging herein). In direct imaging configuration, the data obtained with the MXI present artifacts

introduced by the density inhomogeneities of each transmissive Be lens from the stack. Some of these structures can be treated by a simple white field correction (i.e., dividing the image of the sample by the white field of image when no sample is present) or by more sophisticated analysis method such as Principal Component Analysis^{41,49}. This is the analysis that is performed in the images in Figs. 4, 6 and 7. However, a large enough number of white field images (the image of the X-rays on the detector when no sample is present) needs to be accumulated in order to improve the correction with a single shot. This is necessary because the Be CRL are chromatic and the FEL bandwidth jitters, which means that a small change of the incoming central photon energy changes the focal length of the stack, effectively changing the magnification onto the detector. A division of a single shot by a white field can thus be challenging. Alternatively, grating-scanning methods^{50,51}, can provide improved phase-retrieval accuracy considering X-ray optics and thus enabling wavefront reconstruction independent of FEL probing beam illumination profile^{52,53}. These abilities further motivate the use of the MXI in combination with Talbot interferometry methods to mitigate these lens artifacts and chromaticity.

Talbot interferometry has been widely used at FELs to determine the wavefront of the X-ray beam, and its focal properties in a single shot^{46,54–56}. The method uses a two dimensional phase diffraction grating placed in the beam. At a specific distance behind the grating self-image^{57,58} of the grating is reproduced. Analysis of the distortions, typically using Fourier methods^{59,60} yields the differential phase in two orthogonal dimensions. These differential phases can be integrated to yield the full wavefront of the beam, and back-propagating to the focus yields the focal properties. It has been an important technique to quantify the focus in experiments where X-ray foci of order 100 nm were required. While Talbot X-ray imaging diagnostics have been developed for HEDP applications using laser-based X-ray illumination^{61–63}, we leverage FEL beams to improve spatial resolution, optimizing the diagnostic sensitivity by combining this Talbot phase measurement technique with the direct imaging. The setup, which can be seen in Fig. 9, is essentially the same as the direct imaging setup, with the addition of a Talbot grating.

A checkerboard π -phase grating with a pitch of 22.5 μm was placed at a distance of 48 cm from the scintillator, which corresponds to the first Talbot order self-image.

The raw image of the shock propagating through 200 μm of silicon with this setup is shown in Fig. 10. For these results, we used a set of 25 Beryllium lenses with a radius of curvature of 50 μm and a photon energy of 8.2 keV.

Both the elastic precursor, as well as the phase transformation to denser shocked state of Si, can be seen in the raw image. Overlaid on this image is the grid pattern introduced by the Talbot grating (a zoomed region is shown in the inset) that is used to measure the phase. The two dimensional fringe pattern is analyzed by standard Fourier methods⁵⁹. There are many ways^{46,64–68} to integrate the differential phase, and get the phase $\phi(x, y)$. Since Talbot imaging is a shearing interferometry method, the resolution will depend on the amount of shear (a combination of the pitch of the Talbot grating and the order used), on the magnification introduced by the Beryllium lenses (the limit of which is highly dependent on photon energy and physical constrains) as well as on the reconstruction method (e.g. the bandwidth of the filter used in the Fourier filtering⁵⁹). Ultimately, it will have a theoretical limit given by the pitch of the grating due to the Nyquist–Shannon sampling theorem.

The sensitivity to phase changes will also depend on these parameters. For example, there is no phase sensitivity at all to phase changes with spatial periods equal to the amount of shear (as defined in Eq. (1)), due to the zero in the transfer function of the shear operator. Therefore, the amount of shear (i.e. Talbot pitch and order) will have to be carefully chosen depending on the features in the samples that experimentalists want to reveal, and with which resolution and sensitivity they want to examine them. The optimal reconstruction method will depend on these choices, and on the amount of noise in the data images. A full treatment and review of the various options is beyond the scope of this paper. In our demonstration experiment, we used the first Talbot order and therefore the shear is small, which gives good phase sensitivity for the high spatial frequencies that sharp shock waves induce, as well as good spatial resolution (at the expensive of sensitivity to lower spatial frequencies). For such a small shear, we can use fast and simple method^{69,70} and approximate the shear operator as:

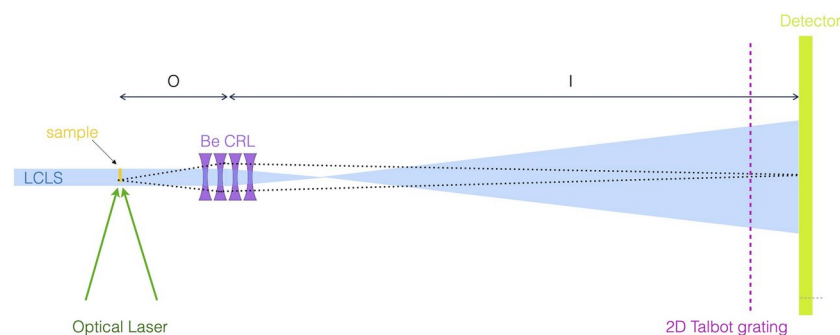


Fig. 9. Talbot Phase Imaging at MEC. The MXI is placed in a direct imaging geometry, where the Be lens stack images the sample onto an X-ray camera. A two dimensional checkerboard π -phase grating is placed at the distance of the first Talbot order before the camera.

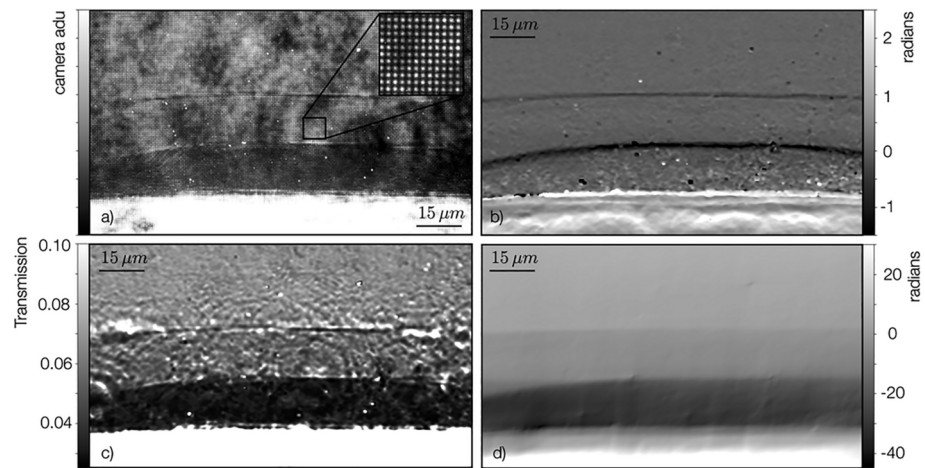


Fig. 10. (a) Raw camera image of a shock in a 200 μm silicon sample, at 8.2 keV. (b) Reconstructed differential phase S_y of Eq. (2). (c) Recovered Transmission of sample. (d) Integrated phase of the sample, $\phi(x, y)$ is Eqs. (1) and (2).

$$S_x(x, y) = \phi(x, y) - \phi(x - s, y) = s \frac{\partial \phi}{\partial x}, \quad (1)$$

$$S_y(x, y) = \phi(x, y) - \phi(x, y - s) = s \frac{\partial \phi}{\partial y}. \quad (2)$$

We then use the Fourier relation:

$$\mathcal{F} \left(\frac{\partial \phi}{\partial x} \right) = ik_x \mathcal{F}(\phi). \quad (3)$$

From this follows:

$$\phi = \mathcal{F}^{-1} \left(\frac{\mathcal{F}(S_x + iS_y)}{ik_x - k_y} \right), \quad (4)$$

which can be efficiently implemented using a fast Fourier transform and its inverse.

We used this method on a shock compressed silicon sample driven by the MEC long pulse laser, as detailed in Fig. 10.

First, an image was taken of the white field illumination (i.e., the beam without a sample in place) to use as a reference. Then, an image of the shocked the sample was taken. Figure 10a shows that raw camera image of the shock, while the reconstructed transmission of the sample is shown in Fig. 10c. The structure that the set of Be lenses introduces is highly visible in both images. Figure 10b shows the differential phase in the y direction, i.e. $S_y(x, y)$ in Eq. (2). In Fig. 10d we show the actual phase, $\phi(x, y)$ introduced by the sample; the structure in the intensity introduced by the lenses disappears, as it is not present in the phase. The phase change behind the elastic wave can clearly be seen, as well as the larger shift after the phase change.

We should note however, that the shock fronts that we image are, at these pressures, expected to be only a few (tens) of atomic layers thick. Since we cannot resolve this, we only measure a jump in the phase at the shock front. Any additional phase jump of an integer multiple of 2π can therefore not be distinguished (e.g. similar to VISAR⁷¹ measurements where only one interferometry arm is used). Additional diagnostics (e.g. VISAR) or prior knowledge of the shock will have to be used to resolve this ambiguity. In the data shown in Fig. 10, with photon energy of 8.2 keV the resolution of the phase measurement is approximately 1.2 μm . We have also successfully tested the method at 17 keV, however with less resolution due the smaller magnification. Since our current scintillator based camera requires a minimum sample transmission of approximately 5%, higher photon energies can be helpful to investigate thicker targets, or higher Z materials. The ultimate limit of resolution that we can likely reach with the MXI at MEC can be much lower than shown in this demonstration experiment: a magnification of up to $\times 40$ at photon energies below 10 keV can be achieved, and combined with a 4 μm Talbot pitch, a resolution of 8 μm in the phase measurement at the detector or $\frac{8 \mu\text{m}}{40} = 200 \text{ nm}$ lies within the realms of the possible.

Concluding remarks

In conclusion, we have developed an X-ray imaging diagnostic at MEC that is available to the user community. It can be used in combination with the MEC long pulse laser to, for example, image shock waves and phase transformation in materials over large field of view, and with the MEC short pulse laser system, to image its interaction with dense plasmas at high resolution. The diagnostic has a 200 nm spatial resolution, taking 50 fs (the pulse duration of the FEL) snapshot of excited HED samples, and can operate using photon energies ranging from 5 to 24 keV. In combination with the direct imaging geometry, a Talbot Imaging setup can be used to measure both intensity and phase changes introduced by a target with sub-micron resolution.

Data availability

The datasets used and analyzed during the current study are available from the corresponding author on reasonable request.

Received: 7 November 2024; Accepted: 24 February 2025

Published online: 04 March 2025

References

- Katayama, M., Shiraga, H., Nakai, M., Kobayashi, T. & Kato, Y. 4.8-keV X-ray backlight framing method for observing images of soft-X-ray-driven fusion capsules. *Rev. Sci. Instrum.* **64**, 706. <https://doi.org/10.1063/1.1144202> (1993).
- Kalantar, D. H. et al. X-ray backlit imaging measurement of in-flight pusher density for an indirect drive capsule implosion. *Rev. Sci. Instrum.* **68**, 814. <https://doi.org/10.1063/1.1147696> (1997).
- Marshall, F. J. et al. Plasma-density determination from X-ray radiography of laser-driven spherical implosions. *Phys. Rev. Lett.* **102**, 1. <https://doi.org/10.1103/PhysRevLett.102.185004> (2009).
- Hicks, D. G. et al. Streaked radiography measurements of convergent ablator performance. *Rev. Sci. Instrum.* **81**, 727. <https://doi.org/10.1063/1.3475727> (2010).
- Dewald, E. L. et al. X-ray streaked refraction enhanced radiography for inferring inflight density gradients in ICF capsule implosions. *Rev. Sci. Instrum.* **89**, 10G108. <https://doi.org/10.1063/1.5039346> (2018).
- Do, A. et al. Direct measurement of ice-ablator interface motion for instability mitigation in indirect drive ICF implosions. *Phys. Rev. Lett.* **129**, 215003. <https://doi.org/10.1103/PhysRevLett.129.215003> (2022).
- Montgomery, D. S. Invited article: X-ray phase contrast imaging in inertial confinement fusion and high energy density research. *Rev. Sci. Instrum.* **94**, 021103 (2023).
- Shelkovenko, T. A., Sinars, D. B., Pikuz, S. A. & Hammer, D. A. Radiographic and spectroscopic studies of X-pinch plasma implosion dynamics and X-ray burst emission characteristics. *Phys. Plasmas* **8**, 1305. <https://doi.org/10.1063/1.1351553> (2001).
- Shelkovenko, T. A., Pikuz, S. A. & Hammer, D. A. A review of projection radiography of plasma and biological objects in X-pinch radiation. *Plasma Phys. Rep.* **42**, 226. <https://doi.org/10.1134/S1063780X16030065> (2016).
- Pikuz, S. A., Shelkovenko, T. & Hammer, D. X-pinch. Part I. *Plasma Phys. Rep.* **41**, 291. <https://doi.org/10.1134/S1063780X15040054> (2015).
- Pikuz, S. A., Shelkovenko, T. & Hammer, D. X-pinch. Part II. *Plasma Phys. Rep.* **41**, 445. <https://doi.org/10.1134/S1063780X15060045> (2015).
- Landen, O. L. et al. X-ray backlighting for the national ignition facility (invited). *Rev. Sci. Instrum.* **72**, 627. <https://doi.org/10.1063/1.1315641> (2001).
- Oliver, M. et al. Diffraction enhanced imaging utilizing a laser produced X-ray source. *Rev. Sci. Instrum.* **93**, 093502. <https://doi.org/10.1063/5.0091348> (2022).
- Morace, A. et al. Development of X-ray radiography for high energy density physics. *Phys. Plasmas* **21**, 102712. <https://doi.org/10.1063/1.4900867> (2014).
- Montgomery, D. S., Nobile, A. & Walsh, P. J. Characterization of national ignition facility cryogenic beryllium capsules using X-ray phase contrast imaging. *Rev. Sci. Instrum.* **75**, 3986. <https://doi.org/10.1063/1.1790054> (2004).
- Kozioziemski, B. J. et al. X-ray imaging of cryogenic deuterium–tritium layers in a beryllium shell. *J. Appl. Phys.* **98**, 903. <https://doi.org/10.1063/1.2133903> (2005).
- Koch, J. A. et al. Refraction-enhanced X-ray radiography for inertial confinement fusion and laser-produced plasma applications. *J. Appl. Phys.* **105**, 92. <https://doi.org/10.1063/1.3133092> (2009).
- Ping, Y. et al. Refraction-enhanced X-ray radiography for density profile measurements at CH/Be interface. *J. Instrum.* **6**, P09004. <https://doi.org/10.1088/1748-0221/6/09/P09004> (2011).
- Workman, J. et al. Phase-contrast imaging using ultrafast X-rays in laser-shocked materials. *Rev. Sci. Instrum.* **81**, 10E520. <https://doi.org/10.1063/1.3485109> (2010).
- Flippo, K. A. et al. Development of a big area backlighter for high energy density experiments. *Rev. Sci. Instrum.* **85**, 093501. <https://doi.org/10.1063/1.4893349> (2014).
- Koch, J. A. et al. Refraction-enhanced backlit imaging of axially symmetric inertial confinement fusion plasmas. *Appl. Opt.* **52**, 3538. <https://doi.org/10.1364/AO.52.003538> (2013).
- Do, A. et al. X-ray imaging of Rayleigh–Taylor instabilities using Fresnel zone plate at the National Ignition Facility. *Rev. Sci. Instrum.* **92**, 053511. <https://doi.org/10.1063/5.0043682> (2021).
- Antonelli, L. et al. X-ray phase-contrast imaging of strong shocks on OMEGA EP. *Rev. Sci. Instrum.* **95**, 113504. <https://doi.org/10.1063/5.0168059> (2024).
- Nugent, K., Gureyev, T., Cookson, D., Paganin, D. & Barnea, Z. Quantitative phase imaging using hard X rays. *Phys. Rev. Lett.* **77**, 2961. <https://doi.org/10.1103/PhysRevLett.77.2961> (1996).
- Cloetens, P. et al. Hard X-ray phase imaging using simple propagation of a coherent synchrotron radiation beam. *J. Phys. D Appl. Phys.* **32**, A145. <https://doi.org/10.1088/0022-3727/32/10A/330> (1999).
- Emma, P. et al. First lasing and operation of an ångström-wavelength free-electron laser. *Nat. Photon.* **4**, 641. <https://doi.org/10.1038/nphoton.2010.176> (2010).
- Nagler, B. et al. The matter in extreme conditions instrument at the linac coherent light source. *J. Synchrotron Radiat.* **22**, 520. <https://doi.org/10.1107/S1600577515004865> (2015).
- Snigirev, A., Kohn, V., Snigireva, I. & Lengeler, B. A compound refractive lens for focusing high-energy X-rays. *Nature* **384**, 49. <https://doi.org/10.1038/384049a0> (1996).
- Lengeler, B. et al. A microscope for hard X-rays based on refractive optics. *Synchrotron Radiat. News* **12**, 45. <https://doi.org/10.1080/08940889908261039> (1999).
- Lengeler, B. et al. Imaging by parabolic refractive lenses in the hard X-ray range. *J. Synchrotron Radiat.* **6**, 1153. <https://doi.org/10.1107/S0909049599009747> (1999).

31. Lengeler, B. et al. Parabolic refractive X-ray lenses. *J. Synchrotron Radiat.* **9**, 119. <https://doi.org/10.1107/S0909049502003436> (2002).
32. Nagler, B. et al. The phase-contrast imaging instrument at the matter in extreme conditions endstation at LCLS. *Rev. Sci. Instrum.* **87**, 103701. <https://doi.org/10.1063/1.4963906> (2016).
33. Schropp, A. et al. Full spatial characterization of a nanofocused X-ray free-electron laser beam by ptychographic imaging. *Sci. Rep.* **3**, 1633. <https://doi.org/10.1038/srep01633> (2013).
34. Seiboth, F. et al. Perfect X-ray focusing via fitting corrective glasses to aberrated optics. *Nat. Commun.* **8**, 14623. <https://doi.org/10.1038/ncomms14623> (2017).
35. Barker, L. M. & Hollenbach, R. E. Laser interferometer for measuring high velocities of any reflecting surface. *J. Appl. Phys.* **43**, 4669. <https://doi.org/10.1063/1.1660986> (1972).
36. Schropp, A. et al. Hard X-ray nanobeam characterization by coherent diffraction microscopy. *Appl. Phys. Lett.* **96**, 10. <https://doi.org/10.1063/1.3332591> (2010).
37. Optique Peter. <https://www.optiquepeter.com/en/index.php> (2012).
38. Advanced hCMOS Systems. <https://www.hcmos.com/> (2012).
39. Hart, P. A. et al. In *X-ray Free-Electron Lasers: Advances in Source Development and Instrumentation* (Tschechschner, T. et al.) Vol. 11038, 110380Q. <https://doi.org/10.1117/12.2520974> (SPIE, 2019).
40. Looker, Q., Colombo, A. P., Kimmel, M. & Porter, J. L. X-ray characterization of the Icarus ultrafast X-ray imager. *Rev. Sci. Instrum.* **91**, 043502. <https://doi.org/10.1063/5.0004711> (2020).
41. Hodge, D. S. et al. Multi-frame, ultrafast, X-ray microscope for imaging shockwave dynamics. *Opt. Express* **30**, 38405. <https://doi.org/10.1364/OE.472275> (2022).
42. Decker, F.-J. et al. Tunable X-ray free electron laser multi-pulses with nanosecond separation. *Sci. Rep.* **12**, 3253. <https://doi.org/10.1038/s41598-022-06754-y> (2022).
43. Halavanau, A. et al. LCLS multi-bunch improvement plan. In *Proc. IPAC'21, International Particle Accelerator Conference No. 12* 365–368. <https://doi.org/10.18429/JACoW-IPAC2021-MOPAB098> (JACoW Publishing, 2021).
44. Schropp, A. et al. Imaging shock waves in diamond with both high temporal and spatial resolution at an XFEL. *Sci. Rep.* **5**, 11089. <https://doi.org/10.1038/srep11089> (2015).
45. Brown, S. B. et al. Direct imaging of ultrafast lattice dynamics. *Sci. Adv.* **5**, 44. <https://doi.org/10.1126/sciadv.aau8044> (2019).
46. Seaberg, M. et al. Wavefront sensing at X-ray free-electron lasers. *J. Synchrotron Radiat.* **26**, 1115. <https://doi.org/10.1107/S1600577119005721> (2019).
47. Momose, A. et al. Demonstration of X-ray Talbot interferometry. *Jpn. J. Appl. Phys.* **42**, L866. <https://doi.org/10.1143/JJAP.42.L866> (2003).
48. Sato, G. et al. Single-shot X-ray phase-contrast imaging using two-dimensional gratings. In *AIP Conference Proceedings*, Vol. 1466, 29–34. <https://doi.org/10.1063/1.4742265> (American Institute of Physics, 2012).
49. Hagemann, J. et al. Single-pulse phase-contrast imaging at free-electron lasers in the hard X-ray regime. *J. Synchrotron Radiat.* **28**, 52. <https://doi.org/10.1107/S160057752001557X> (2021).
50. Kottler, C., Pfeiffer, F., Bunk, O., Grünzweig, C. & David, C. Grating interferometer based scanning setup for hard X-ray phase contrast imaging. *Rev. Sci. Instrum.* **78**, 043710. <https://doi.org/10.1063/1.2723064> (2007).
51. Zanette, L., Bech, M., Pfeiffer, F. & Weitkamp, T. Interlaced phase stepping in phase-contrast X-ray tomography. *Appl. Phys. Lett.* **98**, 094101. <https://doi.org/10.1063/1.3559849> (2011).
52. Valdivia, M. P. et al. Talbot–Lau X-ray deflectometry phase-retrieval methods for electron density diagnostics in high-energy density experiments. *Appl. Opt.* **57**, 138. <https://doi.org/10.1364/AO.57.000138> (2018).
53. Pérez-Callejo, L. et al. Phase imaging of irradiated foils at the OMEGA EP facility using phase-stepping X-ray Talbot–Lau deflectometry. *High Power Laser Sci. Eng.* **11**, e49. <https://doi.org/10.1017/hpl.2023.44> (2023).
54. Liu, Y. et al. High-accuracy wavefront sensing for X-ray free electron lasers. *Optica* **5**, 967. <https://doi.org/10.1364/OPTICA.5.000967> (2018).
55. Matsuyama, S. et al. Wavefront measurement for a hard-X-ray nanobeam using single-grating interferometry. *Opt. Express* **20**, 24977. <https://doi.org/10.1364/OE.20.024977> (2012).
56. Victorien, B. et al. In *APS Division of Plasma Physics Meeting Abstracts, APS Meeting Abstracts, Development of Talbot–Lau Interferometry for the Study of Laser Generated HED Plasmas at SACLA XFEL*, Vol. 2021, UO06.012. <https://ui.adsabs.harvard.edu/abs/2021APS..DPPUO6012V> (2021).
57. Talbot, H. LXXVI. Facts relating to optical science. No. IV. *Philos. Mag. J. Sci.* **9**, 401. <https://doi.org/10.1080/14786443608649032> (1836).
58. Rayleigh, L. XXV. On copying diffraction-gratings, and on some phenomena connected therewith. *Philos. Mag. J. Sci.* **11**, 196. <https://doi.org/10.1080/14786448108626995> (1881).
59. Takeda, M., Ina, H. & Kobayashi, S. Fourier-transform method of fringe-pattern analysis for computer-based topography and interferometry. *J. Opt. Soc. Am.* **72**, 156. <https://doi.org/10.1364/JOSA.72.000156> (1982).
60. Pérez-Callejo, G. et al. TIA: A forward model and analyzer for Talbot interferometry experiments of dense plasmas. *Phys. Plasmas* **29**, 043901. <https://doi.org/10.1063/5.0085822> (2022).
61. Valdivia, M. P. et al. Talbot-Lau X-ray deflectometer: Refraction-based HEDP imaging diagnostic. *Rev. Sci. Instrum.* **92**, 065110. <https://doi.org/10.1063/5.0043655> (2021).
62. Valdivia, M. P. et al. Current advances on Talbot–Lau X-ray imaging diagnostics for high energy density experiments (invited). *Rev. Sci. Instrum.* **93**, 115102. <https://doi.org/10.1063/5.0101865> (2022).
63. Begishev, I. et al. Referenceless, grating-based, single shot X-ray phase contrast imaging with optimized laser-driven K- α sources. *Opt. Express* **32**, 34694 (2024).
64. Elster, C. Recovering wavefronts from difference measurements in lateral shearing interferometry. *J. Comput. Appl. Math.* **110**, 177. [https://doi.org/10.1016/S0377-0427\(99\)00232-0](https://doi.org/10.1016/S0377-0427(99)00232-0) (1999).
65. Elster, C. & Weingärtner, I. Exact wave-front reconstruction from two lateral shearing interferograms. *J. Opt. Soc. Am. A* **16**, 2281. <https://doi.org/10.1364/JOSAA.16.002281> (1999).
66. Elster, C. Exact two-dimensional wave-front reconstruction from lateral shearing interferograms with large shears. *Appl. Opt.* **39**, 5353. <https://doi.org/10.1364/AO.39.005353> (2000).
67. Nagler, B. et al. Focal spot and wavefront sensing of an X-ray free electron laser using Ronchi shearing interferometry. *Sci. Rep.* **7**, 13698. <https://doi.org/10.1038/s41598-017-13710-8> (2017).
68. Makita, M. et al. Double grating shearing interferometry for X-ray free-electron laser beams. *Optica* **7**, 404. <https://doi.org/10.1364/OPTICA.390601> (2020).
69. Kottler, C., David, C., Pfeiffer, F. & Bunk, O. A two-directional approach for grating based differential phase contrast imaging using hard X-rays. *Opt. Express* **15**, 1175. <https://doi.org/10.1364/OE.15.001175> (2007).
70. Morgan, K. S., Paganin, D. M. & Siu, K. K. W. X-ray phase imaging with a paper analyzer. *Appl. Phys. Lett.* **100**, 124102. <https://doi.org/10.1063/1.3694918> (2012).
71. Celliers, P. M. & Millot, M. Imaging velocity interferometer system for any reflector (VISAR) diagnostics for high energy density sciences. *Rev. Sci. Instrum.* **94**, 011101. <https://doi.org/10.1063/5.0123439> (2023).

Acknowledgements

A.E.G. acknowledges support from the LANL Reines LDRD and from the DOE FES ECA, 2019. Use of the Linac Coherent Light Source (LCLS) SLAC National Accelerator Laboratory, was supported by the U.S. Department of Energy Office of Science, Basic Energy Science under Contract No. DE-AC02-76SF00515. The MEC instrument is supported also by the U.S. Department of Energy Office of Science, Fusion Energy Science under Contract No. DE-AC02-76SF00515, FWP 100106. M.P.V. acknowledges support from the US DOE NNSA grant DE-NA0004028. The work of G.P.-C. has been supported by Research Grant No. PID2022-137632OB-I00 from the Spanish Ministry of Science and Innovation.

Author contributions

All authors contributed equally to this work. All authors reviewed the manuscript.

Declarations

Competing interests

The authors declare no competing interests.

Additional information

Correspondence and requests for materials should be addressed to E.G.

Reprints and permissions information is available at www.nature.com/reprints.

Publisher's note Springer Nature remains neutral with regard to jurisdictional claims in published maps and institutional affiliations.

Open Access This article is licensed under a Creative Commons Attribution-NonCommercial-NoDerivatives 4.0 International License, which permits any non-commercial use, sharing, distribution and reproduction in any medium or format, as long as you give appropriate credit to the original author(s) and the source, provide a link to the Creative Commons licence, and indicate if you modified the licensed material. You do not have permission under this licence to share adapted material derived from this article or parts of it. The images or other third party material in this article are included in the article's Creative Commons licence, unless indicated otherwise in a credit line to the material. If material is not included in the article's Creative Commons licence and your intended use is not permitted by statutory regulation or exceeds the permitted use, you will need to obtain permission directly from the copyright holder. To view a copy of this licence, visit <http://creativecommons.org/licenses/by-nc-nd/4.0/>.

© The Author(s) 2025